Global dynamics of high area-to-mass ratios GEO space debris by means of the MEGNO indicator

Valk, Stéphane; Delsate, Nicolas; Lemaître, Anne; Carletti, Timoteo

Published in:
Advances in Space Research

Publication date:
2009

Document Version
Early version, also known as pre-print

Global dynamics of high area-to-mass ratios GEO space debris by means of the MEGNO indicator

S. Valk * , N. Delsate and A. Lemaître and T. Carletti

University of Namur, Département de Mathématique, Unité de Systèmes Dynamiques, 8, Rempart de la Vierge, B-5000, Namur, Belgium

Abstract

In this paper we provide an extensive analysis of the global dynamics of high-area-to-mass ratios geosynchronous (GEO) space debris, applying a recent technique developed by Cincotta et al. (2000), *Mean Exponential Growth factor of Nearby Orbits* (`MEGNO`), which provides an efficient tool to investigate both regular and chaotic components of the phase space.

We compute a stability atlas, for a large set of near-geosynchronous space debris by numerically computing the `MEGNO` indicator, to provide an accurate understanding of the location of stable and unstable orbits as well as the timescale of their exponential divergence in case of chaotic motion. The results improve the analysis presented in Breiter et al. (2005a) notably by considering the particular case of high-area-to-mass ratios space debris. The results indicate that chaotic orbits region can be highly relevant, especially for very high area-to-mass ratios.

Then, we provide some numerical investigations and an analytical theory which lead to a detailed understanding of the resonance structures appearing in the phase space. These analyses bring to the fore a relevant class of secondary resonances on both sides of the well-known pendulum-like pattern of geostationary space debris, leading to complex dynamics of such objects.

Key words: Solar radiation pressure – Space debris – `MEGNO` – Detection of chaos – Long-term evolution – Geosynchronous orbit – High area-to-mass ratios – Secondary resonances

* Corresponding author
Email address: `stephane.valk@fundp.ac.be` (S. Valk).

1 Introduction

Recent optical surveys in high-altitude orbits, performed by the European Space Agency 1 m telescope on Tenerife (Canary islands), have discovered a new unexpected population of 10 cm size space debris near the geostationary region (GEO). These objects sometimes present highly eccentric orbits with eccentricities as high as 0.55 (Schildknecht et al., 2005, 2004). Following the initial guess of Liou and Weaver (2004) who suggest that this new population may be GEO objects with high area-to-mass ratios, recent numerical and analytical investigations were performed to defend this assumption (Anselmo and Pardini, 2005; Liou and Weaver, 2005). In addition, these authors and others, such as Chao (2006) and later Valk et al. (2008) presented some detailed results concerning the short- and long-term evolution of high area-to-mass ratios geosynchronous space debris subjected to direct solar radiation pressure. More specifically, these latter authors mainly focused their attention on the long-term variation of both the eccentricity and the inclination vector. Moreover, some studies concerning the effects of the Earth's shadowing effects on the motion of such space debris were given in Valk and Lemaître (2008).

However, no concern about the intrinsic stability of such uncommon orbits has been given so far. In other words, up to the present, nobody ever dealt with the question to know whether these orbits are really predictable or not on the time scales of their investigations.

The objective of this paper is basically twofold. The first goal is the investigation of the long-term stability of high area-to-mass ratios space debris subjected to the direct solar radiation pressure, by means of the `MEGNO` criterion. Second, still considering high area-to-mass ratios, we bring to the fore a relevant class of additional secondary structures appearing in the phase space.

The paper is organized as follows. In Section 2, we focus our attention to the specification of the underlying model and we give some details about the numerical aspects of the method. In Section 3, for the sake of completeness we dwell upon the detailed definition of the *Mean Exponential Growth factor of Nearby Orbits* indicator, also providing a review of its main properties, in order to understand the behavior of the chaos indicator. Then in Section 4, in the framework of the validation of our implementation, we retrieve the results obtained by Breiter et al. (2005). We also discuss the significance of the time of integration, recently reported by Barrio et al. (2007). In Section 5, we apply the `MEGNO` technique in order to give a insightful understanding of the stability of high area-to-mass ratios space debris. More specifically, we show that the orbits of such peculiar space debris are extremely sensitive to initial condi-

tions, especially with respect to the mean longitude and the semi-major axis. Second, we perform extended analyses, showing that the related 2-dimensional phase space is dominated by chaotic regions, in particular when the area-to-mass ratio is large. In addition, we also provide some results presenting the importance of the initial eccentricity value in the appearance of chaotic region. Finally, in Section 6, we give extensive numerical and analytical investigations of the additional patterns which will be identified as secondary resonances.

2 The model

For the purpose of our study, we consider the modeling of a space debris subjected to the influence of the Earth's gravity field, to both the gravitational perturbations of the Sun and the Moon as well as to the direct solar radiation pressure. As a consequence the differential system of equations governing the dynamics is given by

$$\ddot{\boldsymbol{r}} = \boldsymbol{a}_{\text{pot}} + \boldsymbol{a}_{☾} + \boldsymbol{a}_{\odot} + \boldsymbol{a}_{\text{rp}} \,,$$

where $\boldsymbol{a}_{\text{pot}}$ is the acceleration induced by the Earth's gravity field which can be expressed as the gradient of the following potential

$$U(r,\lambda,\phi) = -\frac{\mu}{r}\sum_{n=0}^{\infty}\sum_{m=0}^{n}\left(\frac{R_e}{r}\right)^n \mathcal{P}_n^m(\sin\phi)(C_{nm}\cos\, m\lambda + S_{nm}\sin\, m\lambda)\,, \quad (1)$$

where the quantities C_{nm} and S_{nm} are the spherical harmonics coefficients of the geopotential. The Earth's gravity field is modelised using the `EGM96` model (Lemoine et al., 1987). In Eq. (1), μ is the gravitational constant of the Earth, R_e is the Earth's equatorial radius and the quantities (r,λ,ϕ) are the geocentric spherical coordinates of the space debris. $\mathcal{P}_n^m$ are the well-known Legendre functions. It is worth noting that the potential (1) is subsequently expressed in Cartesian coordinates by means of the Cunningham algorithm (Cunningham, 1970).

Both the accelerations $\boldsymbol{a}_{☾}$ and $\boldsymbol{a}_{\odot}$ result from the gravity interaction with a third body of mass m_*, where $* = ☾$ and $* = \odot$, and can be expressed with respect to the Earth's center of mass

$$\boldsymbol{a}_* = -\mu_*\left(\frac{\boldsymbol{r}-\boldsymbol{r}_*}{\|\boldsymbol{r}-\boldsymbol{r}_*\|^3} + \frac{\boldsymbol{r}_*}{\|\boldsymbol{r}_*\|^3}\right)\,,$$

where $\boldsymbol{r}$ and $\boldsymbol{r}_*$ are the geocentric coordinates of the space debris and of the mass m_*, respectively. The quantity μ_* is the gravitational constant of the third-body. In our implementation, we choose the high accurate solar system

ephemeris given by the Jet Propulsion Laboratory (JPL) to provide the positions of both the Sun and the Moon (Standish, 1998).

Regarding the direct solar radiation pressure, we assume an hypothetically spherical space debris. The albedo of the Earth is ignored and the Earth's shadowing effects are not taken into account either. The acceleration induced by the direct solar radiation pressure is given by

$$\mathbf{a_{rp}} = C_r\, P_r \left[\frac{a_\odot}{\|\mathbf{r}-\mathbf{r}_\odot\|}\right]^2 \frac{A}{m}\,\frac{\mathbf{r}-\mathbf{r}_\odot}{\|\mathbf{r}-\mathbf{r}_\odot\|}\,,$$

where C_r is the adimensional reflectivity coefficient (fixed to 1 further on in this paper) which depends on the optical properties of the space debris surface; $P_r = 4.56 \times 10^{-6}$ N/m^2 is the radiation pressure for an object located at the distance of 1 AU; $a_\odot = 1$ AU is a constant parameter equal to the mean distance between the Sun and the Earth and $\boldsymbol{r}_\odot$ is the geocentric position of the Sun. Finally, the coefficient A/m is the so-called area-to-mass ratio where A and m are the effective cross-section and the mass of the space debris, respectively.

3 The Mean Exponential Growth factor of Nearby Orbits

For the sake of clarity we present in this section the definition and some properties of the MEGNO criterion.

Let $\mathcal{H}(\boldsymbol{p},\boldsymbol{q})$, with $\boldsymbol{p} \in \mathbb{R}^n$, $\boldsymbol{q} \in \mathbb{T}^n$, be a n-degree of freedom Hamiltonian system and let us introduce the compact notation $\boldsymbol{x} = (\boldsymbol{p},\boldsymbol{q}) \in \mathbb{R}^{2n}$ as well as $\boldsymbol{f} = (-\partial\mathcal{H}/\partial\boldsymbol{q}, \partial\mathcal{H}/\partial\boldsymbol{p}) \in \mathbb{R}^{2n}$, then the dynamical system is described by the following set of ordinary differential equations

$$\frac{d}{dt}\boldsymbol{x}(t) = \boldsymbol{f}(\boldsymbol{x}(t),\boldsymbol{\alpha})\,, \qquad \boldsymbol{x} \in \mathbb{R}^{2n}\,, \tag{2}$$

where $\boldsymbol{\alpha}$ is a vector of parameters entirely defined by the model. Let $\phi(t) = \phi(t;\boldsymbol{x}_0,t_0)$ be a solution of the flow defined in Eq. (2) with initial conditions $(t_0,\boldsymbol{x}_0)$, then it has associated the Lyapunov Characteristic Number (hereafter LCN), defined by (Benettin et al., 1980)

$$\lambda = \lim_{t\to\infty} \frac{1}{t}\,\ln\frac{\|\boldsymbol{\delta}_\phi(t)\|}{\|\boldsymbol{\delta}_\phi(t_0)\|}, \tag{3}$$

where $\boldsymbol{\delta}_\phi(t)$, the so-called *tangent vector*, measures the evolution of an initial

small deviation $\boldsymbol{\delta}_\phi(t_0) \equiv \boldsymbol{\delta}_0$ between $\phi(t)$ and a nearby orbit, and whose evolution is given by the variational equations (terms of order $\mathcal{O}(\boldsymbol{\delta}^2)$ are omitted)

$$\dot{\boldsymbol{\delta}}_\phi = \frac{d}{dt}\boldsymbol{\delta}_\phi(t) = \boldsymbol{J}(\phi(t))\,\boldsymbol{\delta}_\phi(t)\,, \quad \text{with} \quad \boldsymbol{J}(\phi(t)) = \frac{\partial \boldsymbol{f}}{\partial \boldsymbol{x}}(\phi(t))\,, \tag{4}$$

where $\boldsymbol{J}(\phi(t))$ is the Jacobian matrix of the differential system of equations, evaluated on the solution $\phi(t)$. Let us note that the definition of the LCN, given by Eq. (3), can also be written in an integral form

$$\lambda = \lim_{t\to\infty} \frac{1}{t} \int_0^t \frac{\dot{\delta}_\phi(s)}{\delta_\phi(s)}\, ds\,,$$

where $\delta_\phi = \|\boldsymbol{\delta}_\phi\|$, $\dot{\delta}_\phi = \dot{\boldsymbol{\delta}}_\phi \cdot \boldsymbol{\delta}_\phi / \delta_\phi$.

The Mean Exponential Growth factor of Nearby Orbits (hereafter `MEGNO`) $Y_\phi(t)$ is based on a modified time-weighted version of the integral form of the LCN (Cincotta and Simó, 2000). More precisely

$$Y_\phi(t) = \frac{2}{t} \int_0^t \frac{\dot{\delta}_\phi(s)}{\delta_\phi(s)}\, s\, ds\,,$$

as well as its corresponding mean value to get rid of the quasi-periodic oscillation possibly existing in $Y_\phi(t)$

$$\overline{Y}_\phi(t) = \frac{1}{t} \int_0^t Y_\phi(s)\, ds\,.$$

In the following we will omit the explicit dependence of Y and $\overline{Y}$ on the specific orbit ϕ, once this will be clear from the context.

Actually, this latter allows to study the dynamics for long time scales, where generically $\lim_{t\to\infty} Y(t)$ does not converge, while $\lim_{t\to\infty} \overline{Y}(t)$ is well defined (Cincotta et al., 2003). Consequently, the time evolution of $\overline{Y}(t)$ allows to derive the possible divergence of the norm of the tangent vector $\boldsymbol{\delta}(t)$, giving a clear indication of the character of the different orbits. Indeed, for quasi-periodic (regular) orbits, $Y(t)$ oscillates around the value 2 with a linear growth of the separation between nearby orbits. On the other hand, for chaotic (irregular) motion, the modulus of $\boldsymbol{\delta}$ grows exponentially with time, and $Y(t)$ oscillates around a linear divergence line. Cincotta et al. (2003) showed that, for the quasi-periodic regime, $\overline{Y}(t)$ converges to 2, that is a fixed constant, independent of the orbit. Moreover, it has been shown that ordered motions with harmonic oscillations, i.e. orbits very close to a stable periodic orbit, result asymptotically to $\overline{Y}(t) = 0$.

These latter properties can also be used to compute efficiently a good esti-

mation of the LCN, or similarly the Lyapunov time $T_\lambda = 1/\lambda$, by means of a linear least square fit of $\overline{Y}(t)$. Indeed, in the case of an irregular orbit, the time evolution of $\overline{Y}(t)$ may be easily written as

$$\overline{Y}(t) \simeq a_\star\, t + d, \qquad t \to \infty,$$

where $a_\star$ is simply related to the LCN by the relation $a_\star = \lambda/2$ and d is close to zero.

Regarding the numerical computation of the MEGNO indicator, we adopt the same strategy as in Goździewski et al. (2001). To be specific, in addition to the numerical integrations of both the equations of motion and the first order variation equations, we consider the two additional differential equations

$$\frac{d}{dt}y = \frac{\dot{\boldsymbol{\delta}} \cdot \boldsymbol{\delta}}{\boldsymbol{\delta} \cdot \boldsymbol{\delta}}\,, \qquad \frac{d}{dt}w = 2\frac{y}{t}\,, \tag{5}$$

which allow to derive the MEGNO indicators as

$$Y(t) = 2\,y(t)/t, \qquad \overline{Y}(t) = w(t)/t\,.$$

The MEGNO criterion, unlike the common Lyapunov variational methods, takes advantage of all the dynamical informations for the orbits and the evolution of its tangent vector, which results in shorter times of integration, to achieve comparable results. Moreover, a couple of applications found in the literature (e.g. Goździewski et al. 2001, 2008; Breiter et al. 2005; Cincotta and Simó 2000 justify and confirm that the MEGNO is relevant, reliable and provides an efficient way for the investigation of the dynamics by detecting regular as well as stochastic regimes.

3.1 MEGNO and numerical integrations

As previously mentioned, in order to evaluate the MEGNO indicator, we have to integrate the differential system of equations of motion (2), the linear first order variational system of equations (4) as well as the two additional differential equations (5). We choose to write both the expressions of the perturbing forces and the variational system, i.e. the Jacobian matrix, in rectangular coordinates *positions-velocities*. In such a way we can overcome both the null eccentricity and the null inclination singularity present in the dynamics of space debris (Valk et al., submitted for publication). Moreover the explicit analytical expressions of the vector fields allows us to avoid the difficulties inherent in the classical method of neighboring trajectories (two particles method).

In order to numerically integrate the two differential systems of equations, we adopted the variable step size Bulirsh-Stoer algorithm (see e.g. Bulirsh and

Stoer 1966 and Stoer and Bulirsch 1980). Let us note that, for the purpose of validation, the numerical integrations were also made with a couple of other numerical integrators. However, the Bulirsh-Stoer algorithm seems to be the best compromise between accuracy and efficiency. Moreover, as quoted by Wisdom (1983): *What is more important for this study, Benettin et al. (1980) found that the maximum LCE did not depend on the precision of their calculation. It appears likely that as long as a certain minimum precision is kept, maximum LCE's may be accurately computed, even though it is not possible to precisely follow a specified trajectory for the required length of time.*

Although this latter observation was formulated in the framework of both Lyapunov variational method and Hamiltonian systems, it seems that it remains relevant in the computation of the MEGNO criterion, at least in the particular case of our analysis.

3.2 Influence of the initial tangent vector $\boldsymbol{\delta}_0$

By construction MEGNO depends on the initial value of the tangent vector $\boldsymbol{\delta}_0$, although the latter does not influence significantly the detection of chaotic region. Nevertheless we preferred to adopt the strategy of initialize randomly the initial tangent vectors in order to avoid some parts of *artificially created zones of low MEGNO due to the proximity of $\boldsymbol{\delta}_0$ to the minimum Lyapunov exponent direction* (Breiter et al., 2005). Moreover, as pointed out by Goździewski et al. (2001), the random sampling of $\boldsymbol{\delta_0}$ is relevant in the sense that different initial tangent vectors can lead to different behaviors of the MEGNO time evolution while considering the same orbit. This observation has been reported in the framework of extra-solar planetary systems and seems to remain similar in the case of Earth orbiting objects and more generally for high-dimensional dynamical systems (having more than 3 degrees of freedom).

Regarding the impact of the choice of the initial tangent vector $\boldsymbol{\delta}_0$, we performed a set of exhaustive numerical investigations of regular orbits. More specifically, we compared the time-evolution of the MEGNO using different initial tangent vectors and identical generic initial conditions. The results confirm that the random choice of the initial tangent vector induce a significant random behavior in the way MEGNO approaches the limit value 2, hence preventing this information from being useful to check the stability/instability character of regular orbits. Actually, when considering a slightly perturbed two-body problem (such as the central attraction disturbed by the oblateness of the Earth), the way MEGNO converge to 2 is completely unpredictable , leading to more or less 50% of convergence of $\overline{Y}(t)$ to 2 from above and the other remaining 50% from below. This result is formally discussed in the following subsections. However, when the order of magnitude of the perturbation

is larger, the result does not completely hold anymore. In particular, when considering the perturbing effects induced by the 1:1 resonance, the MEGNO evolution no longer depends on the random choice of the initial tangent vector. In this latter case, the intrinsic stability of the chosen orbits seems also to dictate the evolution of the MEGNO as reported in Cincotta et al. (2003). More specifically, the stability of the orbit seems to influence the time-evolution of the MEGNO the stronger the orbit is closer to a stable or unstable equilibrium point. For instance, regarding the orbits extremely close to a stable equilibrium point, the MEGNO generally approaches slowly the limit value 2 from below even though some infrequent orbits present a MEGNO convergence from above. Conversely, the orbits initially close to the separatrices generally present a MEGNO approaching the value 2 from above.

3.3 MEGNO for integrable systems

In this paragraph we will study the MEGNO indicator for integrable Hamiltonian systems and we will show that generically (if the system is not isochronous) it always converges to 2, moreover the way $Y(t)$ reaches this limit value, say from higher or lower values, depends only on the choice of the initial tangent vector and not on the orbit itself.

So let us consider an integrable Hamiltonian system and suppose to write it in action-angle variables, $\mathcal{H} = \mathcal{H}(\boldsymbol{p})$, $\boldsymbol{p} \in B \subset \mathbb{R}^n$ denotes the action variables and $\boldsymbol{q} \in \mathbb{T}^n$ denotes the angle variables. Then the Hamiltonian equations are

$$\begin{aligned} \dot{\boldsymbol{p}} &= 0\,, \\ \dot{\boldsymbol{q}} &= \frac{\partial \mathcal{H}}{\partial \boldsymbol{p}} = \boldsymbol{\omega}(\boldsymbol{p})\,. \end{aligned}$$

The tangent space (to a given orbit) can be split into the action direction and angle direction, namely $\boldsymbol{\delta} = (\boldsymbol{\delta}_p, \boldsymbol{\delta}_q)$, thus the variational system can be written as

$$\begin{aligned} \dot{\boldsymbol{\delta}}_p &= 0\,, \\ \dot{\boldsymbol{\delta}}_q &= \frac{\partial^2 \mathcal{H}}{\partial \boldsymbol{p}^2} \boldsymbol{\delta}_p = M(\boldsymbol{p})\, \boldsymbol{\delta}_p\,. \end{aligned}$$

If the system is isochronous then $M \equiv 0$, thus $\boldsymbol{\delta}_p$ and $\boldsymbol{\delta}_q$ are constant and $Y(t) = 0$ for all t. On the other hand, if the system is non-isochronous we get $\boldsymbol{\delta}_p(t) = \boldsymbol{\delta}_p(0)$ and $\boldsymbol{\delta}_q(t) = \boldsymbol{\delta}_q(0) + M(\boldsymbol{p}(0))\, \boldsymbol{\delta}_p(0) t$. To simplify the notations let us introduce

$$M\left(\boldsymbol{p}(0)\right) = M_0, \quad \boldsymbol{\delta}_p(0) = \boldsymbol{\xi}_0 \text{ and } \boldsymbol{\delta}_q(0) = \boldsymbol{\eta}_0\,.$$

Using the definition of MEGNO, we get

$$Y(t) = \frac{1}{t}\int_0^t \frac{(M_0\boldsymbol{\xi}_0)^2 s + M_0\boldsymbol{\xi}_0\cdot\boldsymbol{\eta}_0}{(\boldsymbol{\xi}_0)^2 + (\boldsymbol{\eta}_0)^2 + 2M_0\boldsymbol{\xi}_0\cdot\boldsymbol{\eta}_0 s + (M_0\boldsymbol{\xi}_0)^2 s^2} s\, ds\,,$$

and this integral can be explicitly computed and we obtain

$$\begin{aligned} Y(t) = 2 &- \frac{M_0\boldsymbol{\xi}_0\cdot\boldsymbol{\eta}_0}{t(M_0\boldsymbol{\xi}_0)^2}\log[1 + 2M_0\boldsymbol{\xi}_0\cdot\boldsymbol{\eta}_0 t + (M_0\boldsymbol{\xi}_0)^2 t^2] + \\ &- \frac{2}{t}\frac{\sqrt{(M_0\boldsymbol{\xi}_0)^2 - (M_0\boldsymbol{\xi}_0\cdot\boldsymbol{\eta}_0)^2}}{(M_0\boldsymbol{\xi}_0)^2}\left[\arctan\frac{M_0\boldsymbol{\xi}_0\cdot\boldsymbol{\eta}_0 + (M_0\boldsymbol{\xi}_0)^2 t^2}{\sqrt{(M_0\boldsymbol{\xi}_0)^2 - (M_0\boldsymbol{\xi}_0\cdot\boldsymbol{\eta}_0)^2}}\right. \\ &- \left.\arctan\frac{M_0\boldsymbol{\xi}_0\cdot\boldsymbol{\eta}_0}{\sqrt{(M_0\boldsymbol{\xi}_0)^2 - (M_0\boldsymbol{\xi}_0\cdot\boldsymbol{\eta}_0)^2}}\right]. \end{aligned} \tag{6}$$

One can check that the square root is well defined, i.e. positive, and thus one can cast (6) into

$$Y(t) = 2 - \frac{M_0\boldsymbol{\xi}_0\cdot\boldsymbol{\eta}_0}{t}F_1(t) - \frac{1}{t}F_2(t)\,,$$

where F_1 and F_2 are positive functions and F_2 is bounded, we can then conclude that

(1) if $M_0\boldsymbol{\xi}_0\cdot\boldsymbol{\eta}_0 > 0$ then $Y(t)$ approaches 2 from below;
(2) if $M_0\boldsymbol{\xi}_0\cdot\boldsymbol{\eta}_0 < 0$ then $Y(t)$ approaches 2 from above, in fact for large t the first contribution dominate the bounded term F_2.

In this last part we will consider if and under which assumptions the previous results concerning the convergence $Y \to 2$ are still valid, for a quasi–integrable Hamiltonian system of the form $H(\boldsymbol{p},\boldsymbol{q},\epsilon) = H_0(\boldsymbol{p}) + \epsilon V(\boldsymbol{p},\boldsymbol{q})$. The main idea is the following, fix $\epsilon > 0$ but small and consider a "non–chaotic"orbit ϕ_ϵ, namely an orbit without a positive Lyapunov exponent (or if you prefer with a bounded MEGNO), then if ϵ is sufficiently small this orbit is a perturbation of an orbit existing also for $\epsilon = 0$, ϕ_0, and we can check that $Y_{\phi_\epsilon} = Y_{\phi_0} + \mathcal{O}(\epsilon)$, hence the smallness of such ϵ–correction cannot change "the way Y goes to 2". More precisely the Hamilton equations are now

$$\begin{aligned} \dot{\boldsymbol{p}} &= -\frac{\partial\mathcal{H}}{\partial\boldsymbol{q}} = -\epsilon\frac{\partial V}{\partial\boldsymbol{q}} \\ \dot{\boldsymbol{q}} &= \frac{\partial\mathcal{H}}{\partial\boldsymbol{p}} = \boldsymbol{\omega}(\boldsymbol{p}) + \epsilon\frac{\partial V}{\partial\boldsymbol{p}}\,, \end{aligned}$$

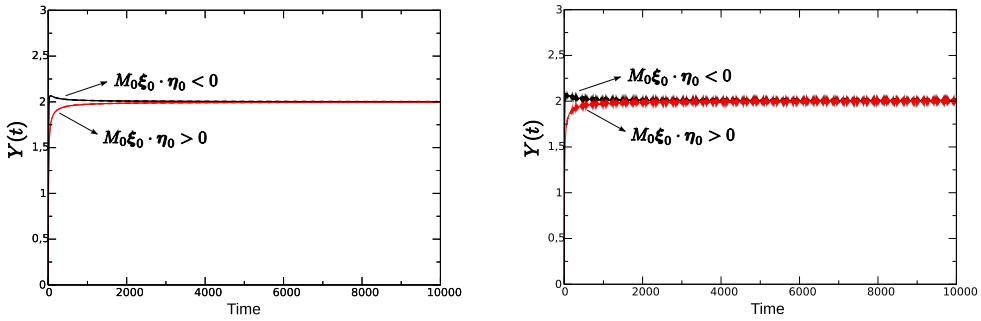

Fig. 1. `MEGNO` for quasi–integrable Hamiltonian system. We consider the evolution of Y_{ϕ_ϵ} for the system $H = p_1^2/2 + p_2 + \epsilon\cos q_1 + \epsilon\cos(q_1 - q_2)$. On the left panel $\epsilon = 10^{-4}$ while on the right panel $\epsilon = 10^{-3}$. In both cases ϵ is small enough to confirm the theoretical predictions, let observe that in this case the matrix M is given by $\left(\begin{smallmatrix} 1 & 0 \\ 0 & 0 \end{smallmatrix}\right)$ and thus the sign condition reads $M\boldsymbol{\delta}_{p,0} \cdot \boldsymbol{\delta}_{q,0} = \delta^1_{p,0}\delta^1_{q,0}$.

and a similar decomposition can be done for the variational system

$$\dot{\boldsymbol{\delta}}_p = -\epsilon\frac{\partial^2 V}{\partial \boldsymbol{p}\partial \boldsymbol{q}}\boldsymbol{\delta}_p - \epsilon\frac{\partial^2 V}{\partial \boldsymbol{q}^2}\boldsymbol{\delta}_q$$
$$\dot{\boldsymbol{\delta}}_q = \left(\frac{\partial^2 \mathcal{H}}{\partial \boldsymbol{p}^2} + \epsilon\frac{\partial^2 V}{\partial \boldsymbol{p}^2}\right)\boldsymbol{\delta}_p + \epsilon\frac{\partial^2 V}{\partial \boldsymbol{p}\partial \boldsymbol{q}}\boldsymbol{\delta}_q\,.$$

Looking for $\boldsymbol{\delta}_p$ and $\boldsymbol{\delta}_q$ as ϵ–power series, i.e. $\boldsymbol{\delta}_p = \boldsymbol{\delta}_{p,0} + \epsilon\boldsymbol{\delta}_{p,1} + \ldots$ and $\boldsymbol{\delta}_q = \boldsymbol{\delta}_{q,0} + \epsilon\boldsymbol{\delta}_{q,1} + \ldots$, and collecting together, in the definition of `MEGNO`, terms contributing to the same power of ϵ, we can thus get

$$Y_{\phi_\epsilon}(t) = \frac{1}{t}\int_0^t \frac{(M_0\boldsymbol{\delta}_{p,0})^2 s + M_0\boldsymbol{\delta}_{p,0}\cdot\boldsymbol{\delta}_{q,0}}{(\boldsymbol{\delta}_{p,0})^2 + (\boldsymbol{\delta}_{p,0})^2 + 2M_0\boldsymbol{\delta}_{p,0}\cdot\boldsymbol{\delta}_{q,0}s + (M_0\boldsymbol{\delta}_{q,0})^2 s^2} s\,ds + \mathcal{O}(\epsilon)$$
$$= Y_{\phi_0}(t) + \mathcal{O}(\epsilon)\,.$$

4 Validation of the method

To validate our method we first apply the technique on a simplified model, containing only the Earth's gravity field expanded up to the second degree and order harmonics, namely, $J_2 = -C_{20}, C_{22}$ and S_{22}. For the purpose of the analysis, we followed a set of 12 600 orbits, propagated over a 30 years time span, that is the order of 10^4 fundamental periods (1 day) empirically required by the method (Goździewski et al., 2001). As reported in Breiter et al. (2005), a 30 years time span seems to be relatively small for long-term investigation of geosynchronous space debris. However, on the one hand, the numerical integration of variational equations in addition to the extrapolation of the orbit

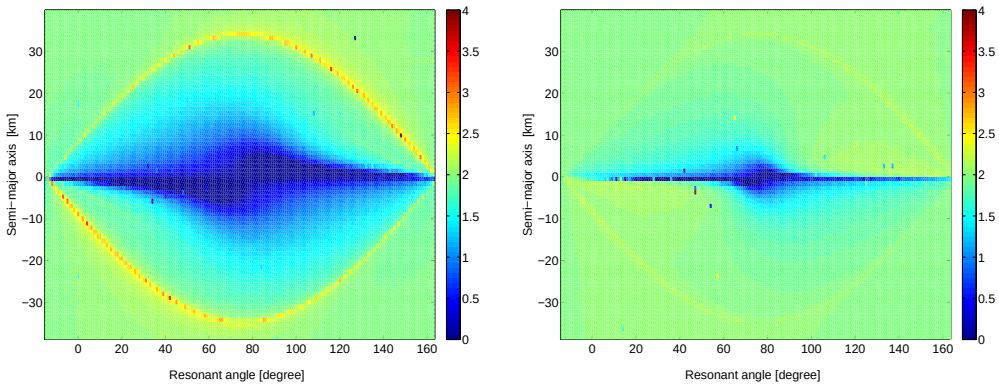

Fig. 2. The MEGNO computed as a function of initial mean longitudes λ_0 and osculating semi-major axis a_0. The equations of motion include the central body attraction as well as the second degree and order harmonics J_2, C_{22} and S_{22}. The mean longitude grid is 1° and the semi-major axis grid is 1 km, spanning the 42164 ± 35 km range. The initial conditions are $e_0 = 0.002$, $i_0 = 0.004$, $\Omega_0 = \omega_0 = 0$. Time at epoch is 25 January 1991. The patterns have been obtained using two different times of integration, $t_f = 30$ years [left] and $t_f = 300$ years [right].

is quite time consuming. Indeed, the simulation with a entry-level step size of 400 seconds takes approximately 20 seconds per orbit when including only the Earth's gravity field whereas it takes 42 seconds with a complete model, which is already significant to examine large sets of initial conditions (typically more than 10^4 orbits). On the other hand, the analysis of the following section, will bring to the fore some indications about the Lyapunov times and it will result smaller than 30 years. As a consequence, the integration time can be considered as sufficiently large in the particular case of our study.

For the purpose of this validation study, we consider a set of initial conditions defined by a mean longitude λ grid of 1°, spanning 90° on both sides of the first stable equilibrium point and a semi-major axis a grid of 1 km, spanning the 42164 ± 35 km range. The other fixed initial conditions are $e_0 = 0.002$ for the eccentricity, $i_0 = 0.004$ for the inclination, $\Omega_0 = \omega_0 = 0$ for the longitude of the ascending node and the argument of perigee, respectively. These values have been fixed to compare our results for the nearly-geosynchronous orbits with the ones of Breiter et al. (2005). As pointed out by Breiter et al. (2005), due to the 1:1 resonance, good variables to present our results will be (a_0, σ_0), where a_0 is the osculating initial semi-axis and σ is the so-called resonant angle, i.e. $\sigma = \lambda - \theta$ with the sidereal time θ.

Figure 2 (left panel) shows the MEGNO values computed using 30 years of integration time. We identify clearly a blow-up of the typical double pendulum-like pattern related to the 1:1 resonance, let observe the horizontal range of 180°. Both the stable and the two unstable equilibrium points are clearly visible.

We observe that the phase space seems to be essentially filled in with MEGNO values $\overline{Y}(t) \simeq 2$, that is plenty of regular orbits. Moreover, the two separatrices are also identifiable and are associated with neighboring MEGNO values $2 < \overline{Y}(t) \leq 4$. Therefore, following the properties defined in Section 3, one could consider that these orbits are chaotic, however, we will show that this conclusion is false. Indeed, a careful identification of the MEGNO time evolution shows that the latter always approach slowly the limit 2 from above. The closer to the separatrice, the slower the convergence. More precisely, none of the above simulated orbits presents a MEGNO time-evolution around a linear divergence line, leading to the conclusion that these orbits are actually unstable periodic orbits, and as a matter of fact also regular.

To clarify this point, we performed a similar study but using a significantly longer time-span, namely 300 years. The results are showed in Figure 2 (right panel). For the sake of comparison, the color bars have been taken identical on both plots. Let us observe that the maximum value reached by the MEGNO is 4 for the left panel and 2.5 for the right one. In the 300 years simulation (Figure 2, right), the MEGNO values, associated with orbits close to the separatrices, turn out to be, on average, smaller than in Figure 2 (left panel), reaching almost the limit $\overline{Y}(t) \to 2$, due to the longer time of integration. Similarly, the dark zone in the neighborhood of the stable equilibrium point corresponding to MEGNO values close to zero, is strongly shrunk, supporting the result that, in the limit of infinitely large t, only the orbit originating from the exact stable equilibrium point leads to $\overline{Y} = 0$ whereas the neighboring trajectories converge slowly to $\overline{Y}(t) = 2$.

Let us note that the importance of integration time has been recently reported by Barrio et al. (2007) in the framework of applications of the MEGNO method, and it is here confirmed. Moreover, the latter paper also underlines some spurious structures appearing in the maps of the variational chaos indicators, explaining the presence of some background patterns (Figure 2), "*suggesting that the same periodic orbit is more or less regular depending on the initial conditions choice*".

5 High area-to-mass ratios analysis

The study of the long-term stability of near-geosynchronous objects has recently received an increasing interest by the scientific community. In the particular case of classical near-geosynchronous objects, the problem has been solved by computing the MEGNO indicator for a family of simulated geostationary, geosynchronous and super-geosynchronous orbits. The concept of classical near-geosynchronous object determines an object the period of which is close to the sidereal day (1 day), subjected by the main gravitational effects of the

Earth, including the 1:1 resonance, the luni-solar perturbing effects as well as the solar radiation pressure for small area-to-mass ratio ($A/m \ll 1$ m^2/kg). According to Breiter et al. (2005) and Wytrzyszczak et al. (2007), the near-geostationary region presents chaotic orbits only very close to the separatrices due to the irregular transits between the libration and the circulation regimes. Regarding the super-geostationary orbits, all the orbits seem to be entirely regular on the time scale of the investigations, that is a few decades.

The aim of this section is to provide a more extensive analysis of the dynamics of near-geosynchronous space debris, subjected to the solar radiation pressure with high area-to-mass ratios (typically $A/m \gg 1$ m^2/kg). Our main objective is to study the effects of high area-to-mass ratios on the stability of the principal periodic orbits and on the chaotic components. This analysis is divided into three parts. First, § 5.1, we focus our attention on the sensitivity to initial conditions; then, § 5.2, we report results of dedicated numerical analyses which emphasize the importance of the area-to-mass ratio value. Finally, in Subsection 5.3, we study the influence of both the initial eccentricity and time at epoch.

Let us recall that for large area-to-mass ratios, the solar radiation pressure becomes the major perturbation, by far larger than the dominant zonal gravity term J_2 (Valk et al., 2008). In this particular case, the larger the area-to-mass ratio, the more affected the dynamics of the near-geosynchronous space debris, leading to daily high-amplitude oscillations of the semi-major axis, yearly oscillations of the eccentricity as well as long-term variations of the inclination. As an illustration, Figure 3 shows the orbital elements histories of the first 210 years of an initial geosynchronous high area-to-mass ratio space debris ($A/m = 10$ m^2/kg). The yearly variation of the eccentricity reaches 0.2, which confirms the expected values predicted by the theories (see e.g. Anselmo and Pardini 2005 and Liou and Weaver 2005). The inclination variation presents a well known long-term variation whose period is directly related to the area-to-mass ratio value. Regarding the longitude of ascending node as well as the argument of perigee, they both present a libration regime due to the chosen set of initial conditions. For further details, we refer to Valk et al. (2008) as well as Chao (2006) where a full description of the long-term motion of high area-to-mass ratios space debris is given.

5.1 Sensitivity to initial conditions

To start with, we follow the evolution of two high area-to-mass ratio space debris ($A/m = 10$ m^2/kg) defined by two sets of very close initial conditions, differing only in the 10th digits in mean longitude. Figure 4 shows the

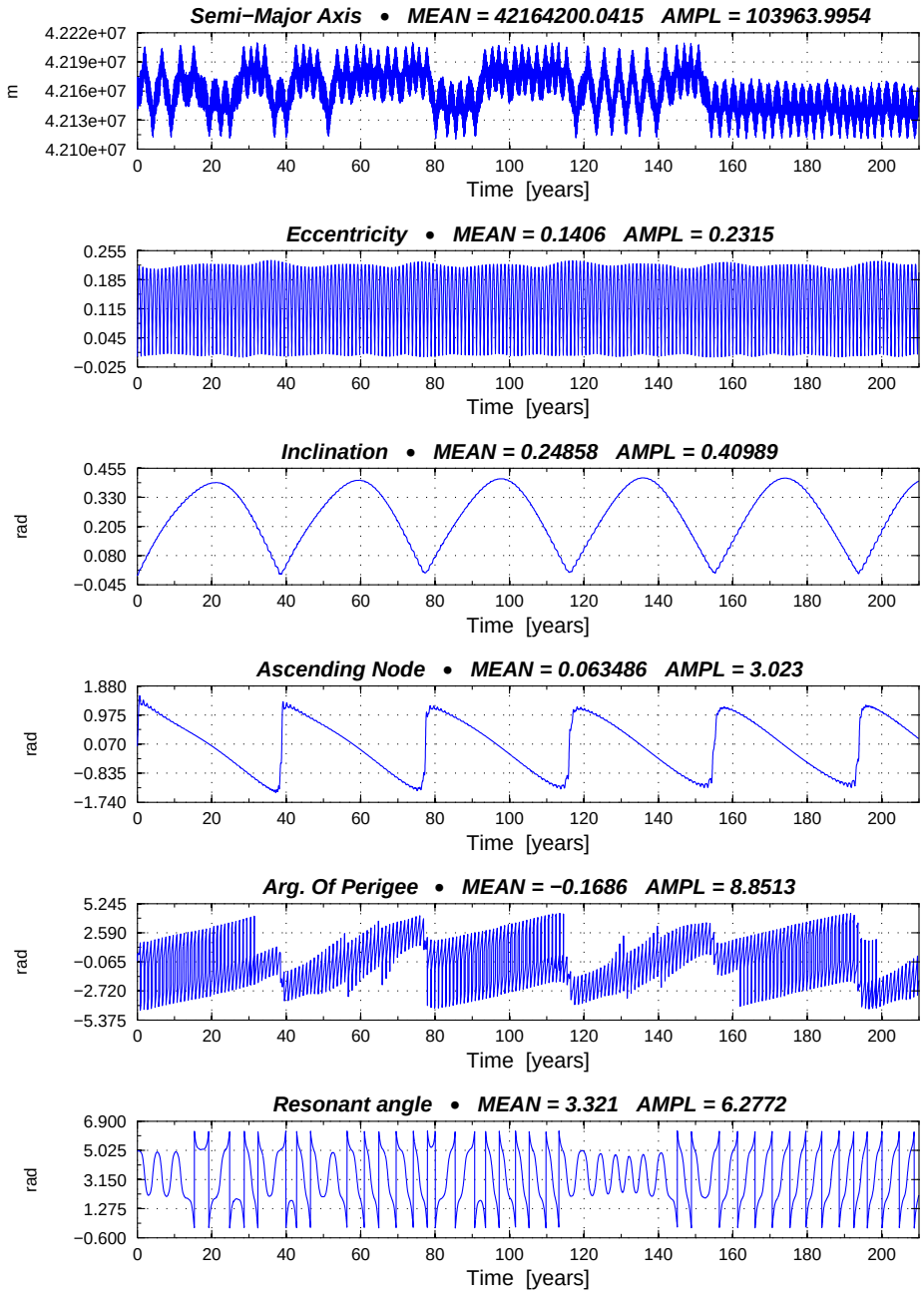

Fig. 3. Time-evolution of the typical high area-to-mass ratio space debris. Orbital elements over 210 years for a $A/m = 10$ m^2/kg, initial conditions are ($a_0 = 42166.473$ km, $e_0 = 0.002, i_0 = 0.004, \Omega_0 = \omega_0 = 0, M_0 = 4.928$). Time at epoch is 25 January 1991.

differences of the dynamical variables for the two orbits, confirming the hypothesis that the sensitivity to initial conditions is especially relevant for the semi-major axis and resonant angle whereas the difference between the other orbital elements remain small. Consequently, we first focus our attention on the time-evolution of the semi-major axis and on the resonant angle. As a complement to Figure 3, we numerically compute two orbits for two space debris with different area-to-mass ratios, $A/m = 1$ m^2/kg and $A/m = 10$ m^2/kg, whose initial condition have been chosen near the separatrices, to emphasize their chaotic behaviours. Figure 5 shows a blow-up of the evolution of the semi-major axis (top panels) and of the resonant angle (middle panels) over the time span of 250 years. It is clear that the semi-major axis present some irregular components over its evolution, related to some transitions between different regimes of motion, clearly identifiable in the resonant angle plots. In addition we also computed the corresponding `MEGNO` time-evolution. The bottom panel in each graph, shows the time-evolution of the `MEGNO` indicator as well as its corresponding mean value.First, we see that the time-evolution of $\overline{Y}(t)$ presents a quasi-linear growth almost since the beginning of the integration process, leading to the conclusion that these orbits are clearly chaotic over that time scale. Therefore, we also computed the linear fit $\overline{Y}(t) \simeq a_\star\, t + d$ in both cases in order to evaluate the Lyapunov time T_λ, by means of the LCN λ or similarly the linear regression coefficients $a_\star = \lambda/2$. Let us remark that to avoid the initial transient state, the least square fits were performed on the last 85% of the time interval. This latter analysis brings to the fore the fact that larger area-to-mass ratios lead to smaller Lyapunov times, i.e. larger Lyapunov Characteristic Number. Indeed, for $A/m = 1$ m^2/kg, the Lyapunov time turns out to be on the order of 11 years whereas it reaches the value $T_\lambda \simeq 3.7$ years for $A/m = 10$ m^2/kg. Second, let us also remark that the behavior of the `MEGNO` indicator is of particular interest in these cases. A careful analysis of $Y(t)$ underlines some irregular patterns directly related to the evolution of σ, in particular when the orbits seem to transit across the separatrices. Finally, we can also highlight the fact that the sudden changes between libration and circulation regimes occur mainly when the inclination changes its sign of variation, especially at the maximum value for $A/m >> 1$ m^2/kg and at the minimum for $A/m \leq 1$ m^2/kg (Figure 5, top panels, dashed line), with an empirical long-term periodicity of T_Ω, that is the long-term periodicity of the longitude of the ascending node which is all the more smaller that A/m is large (Valk et al., 2008).

5.2 Extended numerical analyses

We considered a set of 12 600 simulated orbits with various initial semi-major axes and mean longitudes. All the before-mentioned perturbing effects were taken into account with several values of the area-to-mass ratios regarding

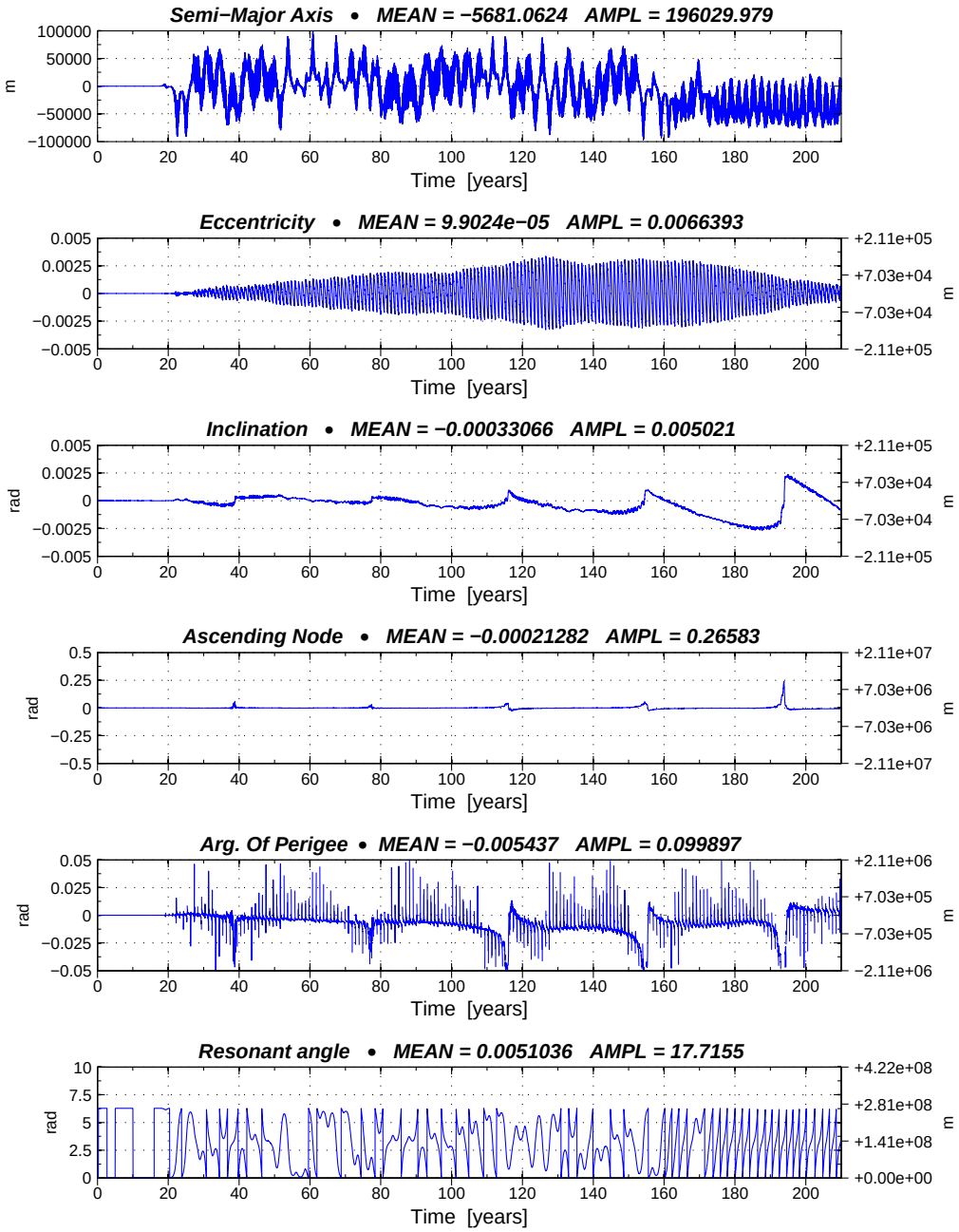

Fig. 4. Effect of sensitivity to initial conditions for high area-to-mass ratio space debris. The figure shows the differences between two orbits with the same initial conditions ($a_0 = 42166.473$ km, $e_0 = 0.002, i_0 = 0.004, \Omega_0 = \omega_0 = 0, M_0 = 4.928$) differing from the 10th digit in mean longitude λ_0. On each graph, the left vertical scale shows the deviations $(\Delta a, \Delta e, \Delta i, \Delta\Omega, \Delta\omega, \Delta\sigma)$ and the right vertical scale the order of magnitude of the difference $(-, a_0\Delta e, a_0\Delta i, a_0\Delta\Omega, a_0\Delta\omega, a_0\Delta\sigma)$ [meters]. Time at epoch is 25 January 1991.

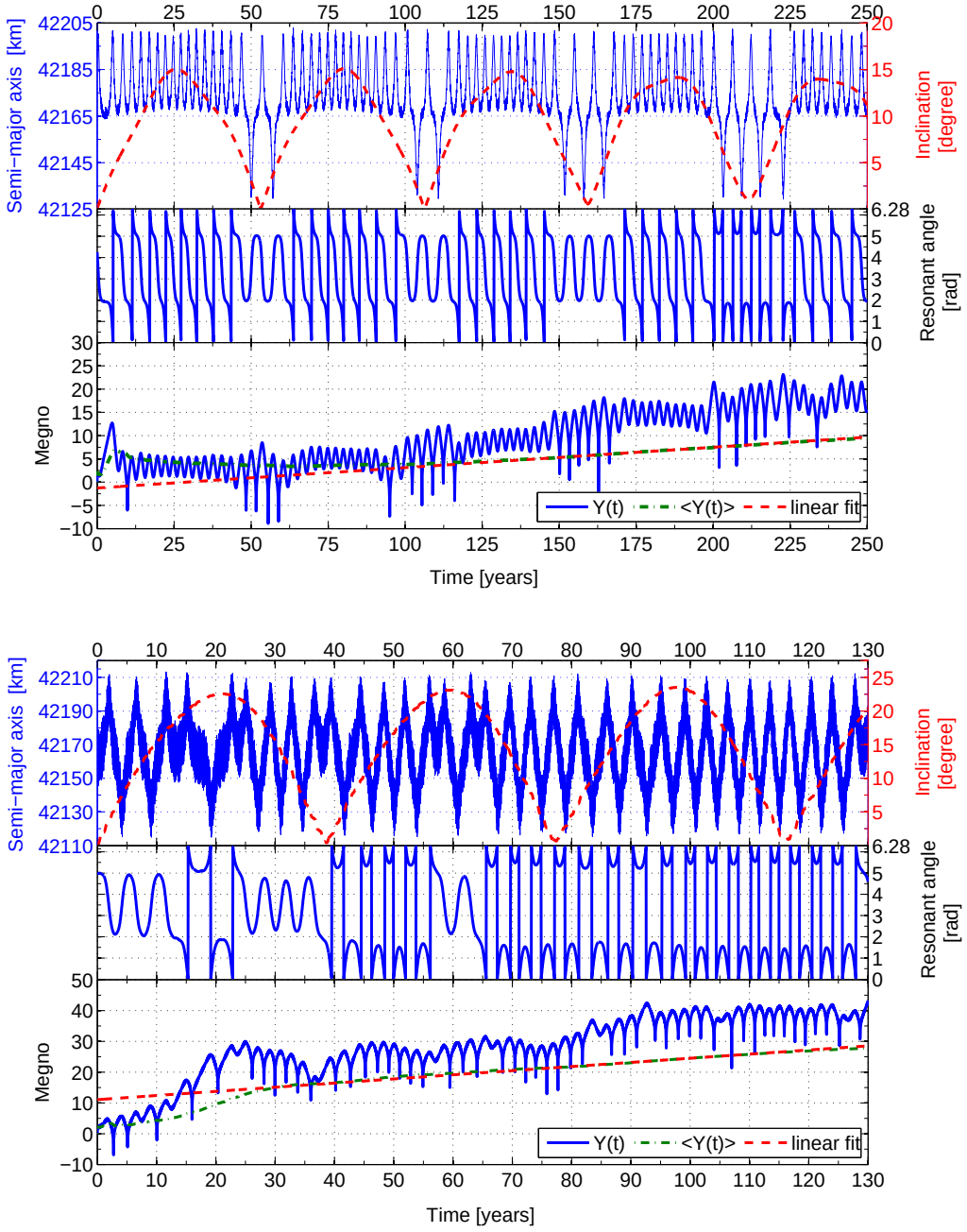

Fig. 5. For each graph, we show the orbital evolution of the semi-major axes a (solid line) superimposed with the evolution of the inclinations (dashed line) [top panels]. The time evolution of the resonant angles [middle panels] and the time-evolution of the MEGNO indicator (Y and $\overline{Y} =< Y(t) >$) as well as the corresponding linear fit $\overline{Y}(t) \simeq a_\star\, t + d$ [bottom panels]. The area-to-mass ratios are $A/m = 1$ m^2/kg in the upper panel and $A/m = 10$ m^2/kg in the lower one. The initial conditions are chosen near the separatrices. The computed linear regression coefficients are given by $a_\star = 0.043$ (for $A/m = 1$ m^2/kg) and $a_\star = 0.134$ (for $A/m = 10$ m^2/kg).

the solar radiation pressure. Results are reported in Figure 6, in the case $A/m = 1$ m^2/kg (top left panel), we recognize the same pendulum-like pattern as in Figure 2. Considering the same integration time (30 years), we notice that the MEGNO values tend to be slightly larger than in Figure 2 (left). Moreover, some irregularly distributed MEGNO values are clearly visible close to the two saddle unstable stationary points. These results completely agree

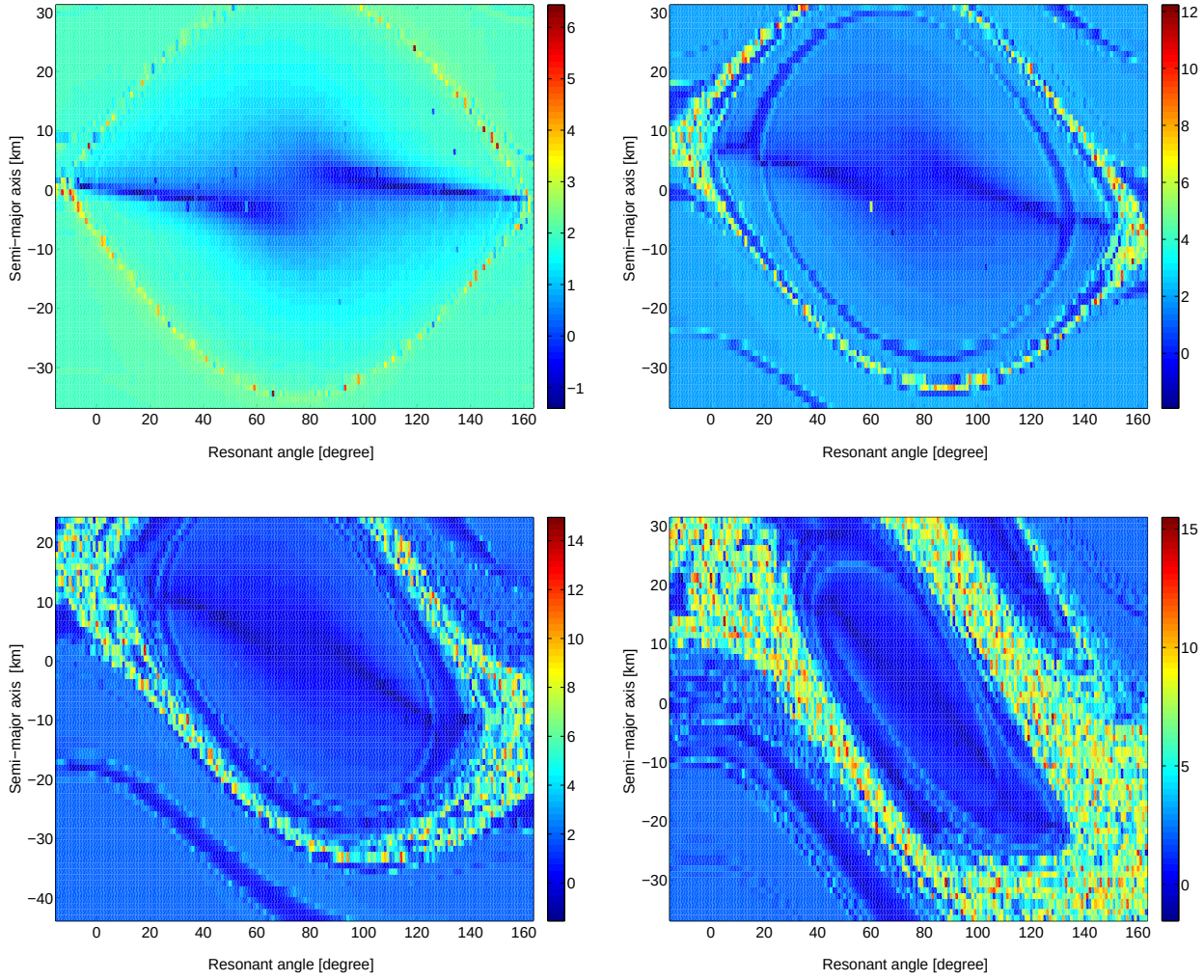

Fig. 6. The MEGNO computed as a function of initial mean longitudes λ_0 and initial (osculating) semi-major axis a_0. The equations of motion include the central body attraction, the second degree and order harmonics J_2, C_{22} and S_{22}, the luni-solar interaction as well as the perturbing effects of the solar radiation pressure. The mean longitude grid is 1° and the semi-major axis grid is 1 km, spanning the 42164 ± 35 km range. The initial conditions are $(e_0 = 0.002, i_0 = 0.004, \Omega_0 = \omega_0 = 0)$. The integration time is 30 years from epoch fixed at 25 January 1991. The patterns have been obtained using four different area-to-mass ratios, $A/m = 1, 5, 10, 20$ m^2/kg, respectively top left, top right, bottom left and bottom right panel.

with those presented by Breiter et al. (2005) where the solar radiation pres-

sure was taken into account but only for very small area-to-mass ratios (typically 0.005 m^2/kg). Indeed, our latter analysis shows that in addition to the luni-solar perturbations, the solar radiation pressure (with small to moderate area-to-mass ratios, that is $0 \leq A/m \leq 1$ m^2/kg), do not change considerably the phase space pattern.

On the other hand the remaining panels of Figure 6 show that the phase portrait becomes significantly more intricate with increasing area-to-mass ratios. Indeed, the width of the stochastic zone in the neighbourhood of the separatrices becomes relevant with a large displacement of the separatrices on the phase plane. The larger chaotic region can readily be explained by the osculating motion of the separatrices due to the before-mentioned daily variations of the semi-major axis with respect to some mean value as well as by the increasing amplitudes of the eccentricities. These variations lead inevitably to transits between both the regions separating libration and circulation motion for orbits initially close to the separatrices.

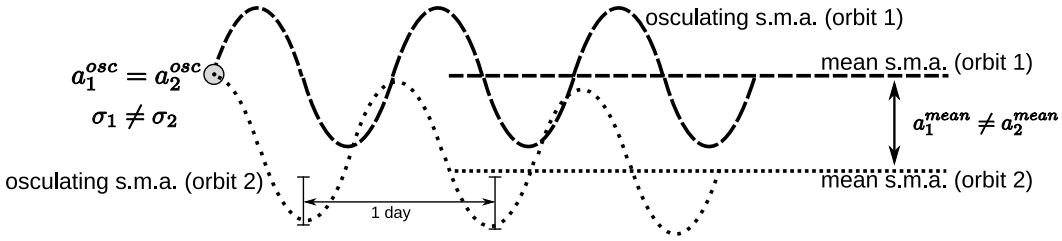

Fig. 7. Cartoon to illustrate the difference between mean and osculating initial conditions with respect to the semi-major axis (s.m.a.) evolution. For the sake of simplicity, the mean semi-major axis does not present any long-term variation whereas the osculating semi-major axis present daily oscillations related to the direct radiation pressure (the implicit underlying model is radiation pressure only). It is clear that even if the osculating initial conditions a_1^{osc} and a_2^{osc} are identical, the corresponding mean initial conditions a_1^{mean} and a_2^{mean} can be significantly different due to different initial mean longitudes (similarly different initial resonant angle values).

Moreover, it is also clear that the usual double pendulum-like phase space shows a tendency to be distorted with a apparent displacement of the unstable equilibrium points whereas the stable equilibrium points remain almost fixed. This last result is however quite awkward insofar as there is no physical interpretation to this phenomenon. Indeed, the direct radiation pressure does not depend explicitly on the resonant angle with respect to the long-term investigations and therefore can not induce a displacement of the equilibrium points in the phase space. Actually, an ingenious explanation can be found regarding the way the sampling is considered in the elaboration of the graphics. More specifically, it is worth noting that, at first, the sampling is carried out with respect to osculating initial conditions. Second, within the framework of mean-motion theory, it is well-known that, due to the short-period oscillations, the mean and the osculating initial conditions can not be considered to be equal. In other words, when considering an horizontal line in the initial

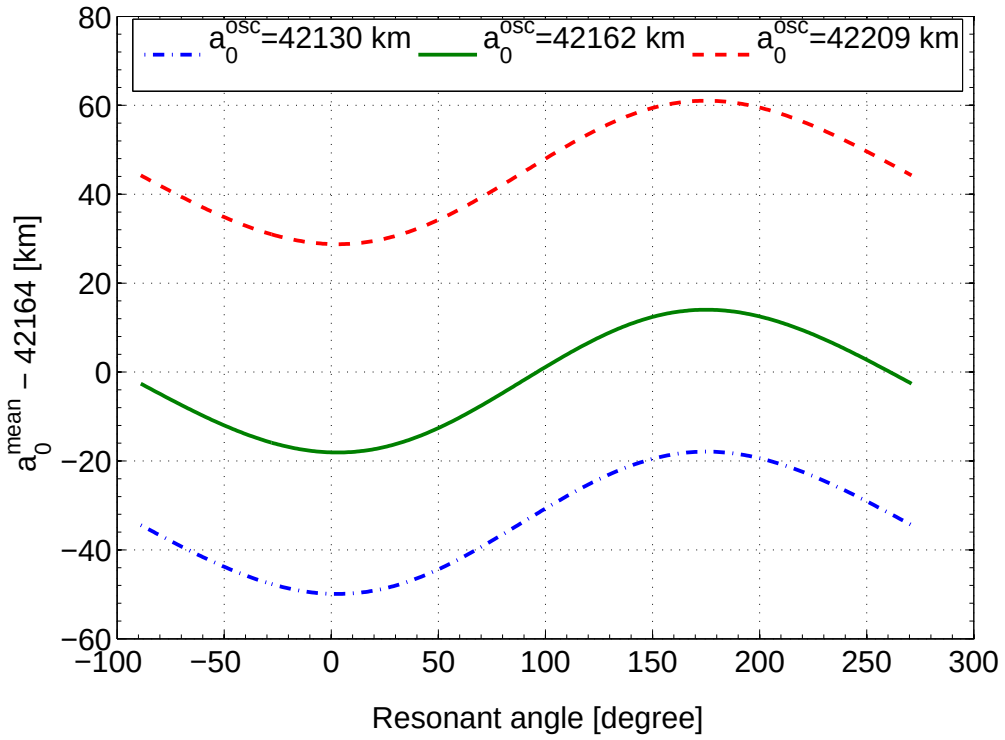

Fig. 8. Relation between the mean semi-major axis and the resonant angle for various values of the osculating semi-major axis. The first osculating semi-major axis is taken above the libration region, the second is related to an osculating semi-major axes sampling which crosses the libration region and finally, the third sampling is taken below this region.

conditions sampling, even though it corresponds to a fixed value of the initial osculating semi-major axis, it is actually related to a various set of mean initial semi-major axis as explained with Figure 7. Actually, the different initial mean longitudes induce a phase difference in the corresponding evolution of the semi-major axis, leading to different mean initial semi-major axes. Let us remark that the maximum difference between both the mean semi-major axes is directly related to the order of magnitude of the short-period variations, and as a consequence, also directly related to the area-to-mas ratio.

More rigorously, the difference between osculating and mean initial conditions is a well-defined transformation, depending on the generating function used within the averaging process allowing to change from mean to osculating dynamics. For further details concerning this explicit transformation, we refer to the Lie algorithm discussed in Deprit (1969) and Henrard (1970). However because we bound our analysis mainly to numerical simulations, we cannot access to such generating function; we can nevertheless overcome this problem by numerically compute, for each semi-major axis osculating initial condition,

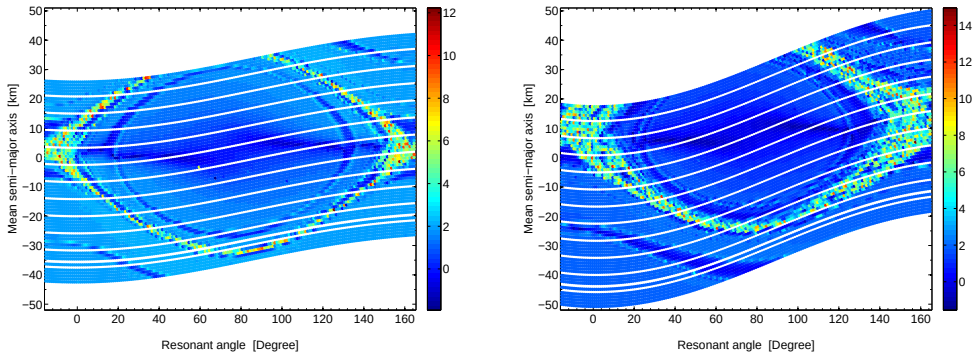

Fig. 9. The MEGNO computed as a function of initial mean longitudes λ_0 and initial mean semi-major axis a_0. The model is the same as in Figure 6. The area-to-mass ratio is, $A/m = 5, 10$ m^2/kg for the left and for the right graph, respectively.

the related mean initial semi-major axis by considering the average over a short time span of 10 days. As an illustration, in Figure 8, we give the relation between the mean semi-major axis and the resonant angle for various values of the osculating semi-major axis ($A/m = 10$ m^2/kg). The first difference is related to a semi-major axis sampling taken above the libration region, the second is related to a semi-major axis sampling which crosses the libration region and finally, the third sampling is taken below this region. In conclusion, we clearly see that the order of magnitude of the differences is, as previously mentioned, the order of the amplitudes of the daily variations observed in the semi-major axis dynamics. Let us note that in the latter case, i.e. $A/m = 10$ m^2/kg, the differences reach at most 27 km which corresponds exactly to the difference between the stable and unstable equilibrium points as shown in Figure 6 (bottom, left).

We can thus numerically apply the transformation as a post-treatment process, that is considering the MEGNO values, not in the osculating initial conditions phase space, but in the mean initial conditions phase space. For the sake of comparison with Figure 6, we show the results once such a transformation has been applied (Figure 9), it is clear that now the vertical gaps between both the stable and unstable equilibrium points, are almost completely eliminated, hence these points have almost the same mean semi-major axis, getting rid of the what we called the "*short-period artefact*".

Let us also remark, that from now on, all the results will be shown in the mean initial conditions phase space.

One should also recall that the solar radiation pressure leads to a theoretical equilibrium defined both in eccentricity e_0 and longitude of perigee ϖ_0. The conditions leading to such an equilibrium can be written as

$$\begin{cases} e_0 = \dfrac{3}{2} C_r P_r \dfrac{A}{m} \dfrac{1}{n\, a\, n_\odot} \cos^2 \dfrac{\epsilon}{2} \simeq 0.01\, C_r \dfrac{A}{m}\,, \\ \varpi_0 = \lambda_\odot(0)\,. \end{cases}$$

where n and $n_\odot$ are the angular motion of both the space debris and the Sun respectively, ϵ is the obliquity of the Earth with respect to the ecliptic and $\lambda_\odot(0)$ the initial ecliptic longitude of the Sun. If these conditions are fulfilled, it has been shown, Chao (2006) and later Valk et al. (2008), that the eccentricity vector $(e\cos\varpi, e\sin\varpi)$ remains constant leading to fixed value of both the eccentricity and longitude of perigee. As an illustration, Figure 10 shows the mid-term variations of the eccentricity for a fixed value of the area-to-mas ratio ($A/m = 10$ m^2/kg) and fixed initial conditions, namely, $a_0 = 42164$ km, $e_0 = 0.1$, $i_0 = 0$ rad, $\Omega_0 = \omega_0 = \lambda_0 = 0$. It is clear that, apart from a phase difference, the amplitudes of variations of the eccentricities are qualitatively the same, except when adopting an initial time at epoch equal to 21 March. In this latter case, the eccentricity remains almost constant, as expected by the theory. Figure 11 shows the phase space in mean semi-major axis and longitude for a fixed value of the area-to-mass ratio $A/m = 10$ m^2/kg and fixed values of initial conditions, namely $e_0 = 0.1$, $i_0 = 0.004$, $\Omega_0 = \omega_0 = 0$. The differences between the two graphs only depends on the initial *time at epoch* parameter t_0. We could actually expect that different initial times at epoch, namely, different initial ecliptic longitudes of the Sun $\lambda_\odot(0)$, will reveal a quite rich collection of behaviors depending on the different states with respect to the before-mentioned *eccentricity equilibrium*. Actually, assuming an initial time at epoch of 21 December 2001, we see clearly that the phase space is filled by a large number of chaotic orbits (Figure 11, left). On the contrary starting with an initial time at epoch of 21 March 2000, that is adopting a Sun pointing longitude of perigee ($\lambda_\odot(0) = 0$ rad), the values reached by the `MEGNO` tend to be smaller associated with significantly narrower chaotic region always located close to the separatrices (Figure 11, right). In the latter case, the eccentricity presents only small yearly variations due to the proximity of the theoretical equilibrium. Therefore, these results seem to suggest that high-amplitude variations of the eccentricity increase considerably the order of magnitude of chaotic region close to the separatrices and conversely, small eccentricity variations seem to considerably minimize the extent of chaotic regions. To justify this assumption, we performed a dedicated numerical simulation with the same set of parameters used in the one reported in Figure 11 but considering higher values of the initial eccentricity. Results are reported in

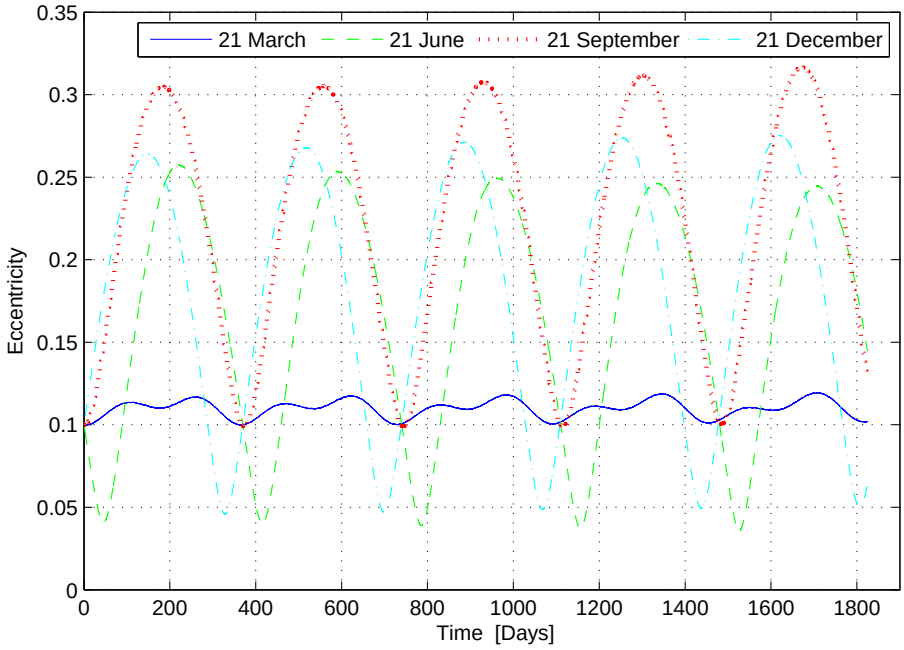

Fig. 10. *Eccentricity equilibrium.* Mid-term variations (yearly oscillations) of the eccentricity for a fixed initial conditions $a_0 = 42164$ km, $e_0 = 0.1$, $i_0 = 0$ rad, $\Omega_0 = \omega_0 = \lambda_0 = 0$ rad and a fixed area-to-mass $A/m = 10$ m^2/kg. Various initial time at epoch t_0, namely different initial ecliptic longitude of the Sun $\lambda_\odot(0)$ were used for the numerical propagations.

Figure 12, the chosen time at epoch is 21 December 2000 and the initial eccentricities are, $e_0 = 0.2$ (left panel) and $e_0 = 0.4$ (right panel). In the latter case, the huge variations of the perigee altitude, induced by the large variations of the eccentricity as well as by the variations of the semi-major axis, leads to even more complicated dynamics. These results confirm thus the importance of the initial eccentricity in the appearance of chaos.

6 Secondary resonances

It is worth noting that inspecting Figures 9, 11 and 12, we clearly note the presence of some additional patterns located on both sides of the separatrices in the phase space. These never seen before regions, unexplained so far, are actually characterized by significant very low `MEGNO` values. Indeed, this observation underlines the fact that the dynamics of high area-to-mass ratios space debris is even more intricate than expected. In the following two paragraphs we will provide some numerical results and a analytical theory based on a simplified model, to better understand such zones.

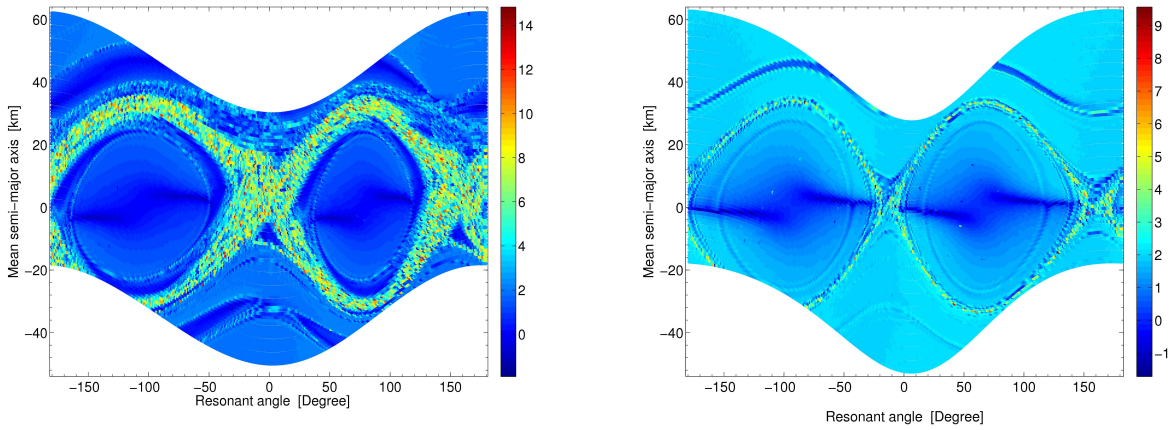

Fig. 11. The MEGNO computed as a function of initial mean longitudes λ_0 and semi–major axis a_0. The equations of motion include the central body attraction, the second degree and order harmonics J_2, C_{22} and S_{22}, the luni-solar interaction as well as the perturbing effects of the solar radiation pressure. The mean longitude grid is 1° and the semi-major axis grid is 1 km spanning the 42164 ± 35 km range. The initial conditions are $e_0 = 0.1, i_0 = 0.004, \Omega_0 = \omega_0 = 0$ with an area-to-mass ratio $A/m = 10$ m^2/kg. The patterns have been obtained using two different initial times at epoch, namely, 21 December 2000 (left), 21 March 2000 (right), respectively.

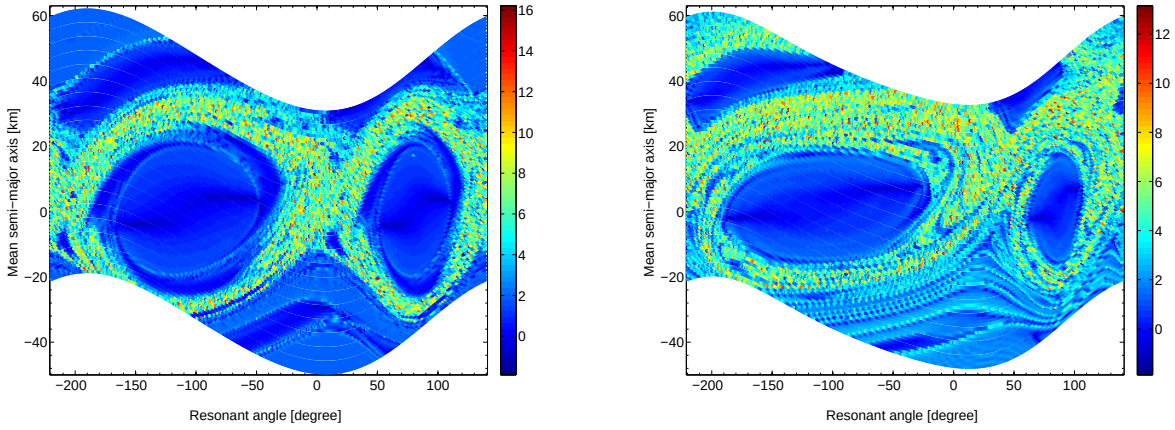

Fig. 12. The MEGNO computed as a function of initial mean longitudes λ_0 and semi–major axis a_0. The equations of motion include the central body attraction, the second degree and order harmonics J_2, C_{22} and S_{22}, the luni-solar interaction as well as the perturbing effects of the solar radiation pressure. The mean longitude grid is 1° and the semi-major axis grid is 1 km spanning the 42164 ± 35 km range. The initial conditions are $i_0 = 0.004$, $\Omega_0 = \omega_0 = 0$ with an area-to-mass ratio $A/m = 10$ m^2/kg. Time at epoch is 21 December 2000. The patterns have been obtained using two initial eccentricities, $e_0 = 0.2$ (left) and $e_0 = 0.4$ (right).

6.1 Numerical investigations

We followed a large set of near-geosynchronous space debris, related to extremely large set of initial conditions taken on both sides of the pendulum-

like pattern, and for each one of the 72 000 orbits we computed the related MEGNO indicator. The initial conditions have been fixed by a mean longitude grid of 1°, spanning 360° and a semi-major axis grid of 1 km spanning the $42\,164 \pm 100$ km range, while the remaining ones and time at epoch are the same as in Figure 6. Moreover, as in the previous extended analyses, the model of forces also includes the central body attraction, the second degree and order harmonics J_2, C_{22} and S_{22} as well as the combined attractions of the Sun and the Moon. The perturbing effects of the direct solar radiation pressure are also taken into account for a high area-to-mass ratio fixed to $A/m = 10$ m^2/kg. Results are reported in Figure 13 which is nothing but an extensive enlargement of the phase space presented in Figure 6 (bottom, left). This phase space widening clearly underlines the before-mentioned additional structures located at $\pm$ 40 km on each side of the resonant area. Furthermore, besides these patterns, what is of special interest is that this Figure also brings to the light supplementary structures located at approximately 80 km on both sides of the main resonance, suggesting that the phase space is actually foliated by a larger set of secondary structures. Moreover, the order of magnitude of these additional patterns seems to be directly related to the inverse of the distance with respect to the resonant area.

In addition, we also performed a set of similar numerical investigations, in order to distinguish qualitatively the relative relevance of some parameters such as the initial mean eccentricity and the value of the area-to-mass ratio. As well as the importance of the 1:1 resonance and of the third-body perturbations in the occurrence of such secondary structures. Even though these results are not presented here in detail, we can draw the following preliminary conclusions: the second order harmonic J_2 as well as the third-body perturbations do not seem to be really relevant and crucial in the appearance of these additional patterns. In other words, the unexpected patterns occur only when taking into account the combined effects of both the second order and degree harmonic and the direct radiation pressure. As a matter of fact, the extended numerical investigations performed in Figure 6 (top, left) or similarly those performed in Breiter et al. (2005) also present these structures even though they are difficult to perceive. Actually, the order of magnitude of the secondary patterns seems to be directly proportional to the area-to-mass ratio value or equivalently directly proportional to the mean value of the eccentricity.

To get even more concluding results, we considered a blow-up of the phase space (dashed line rectangle in Figure 13) with really high-resolution sampling (approximately 150 meters w.r.t. the semi-major a axis and 0.3° w.r.t. the resonant angle σ). Figure 14 (top) shows this phase space widening wherein we defined a so-called *resonant angle section* (horizontal black solid line), that is the subset of orbits having the same initial resonant angle value. This

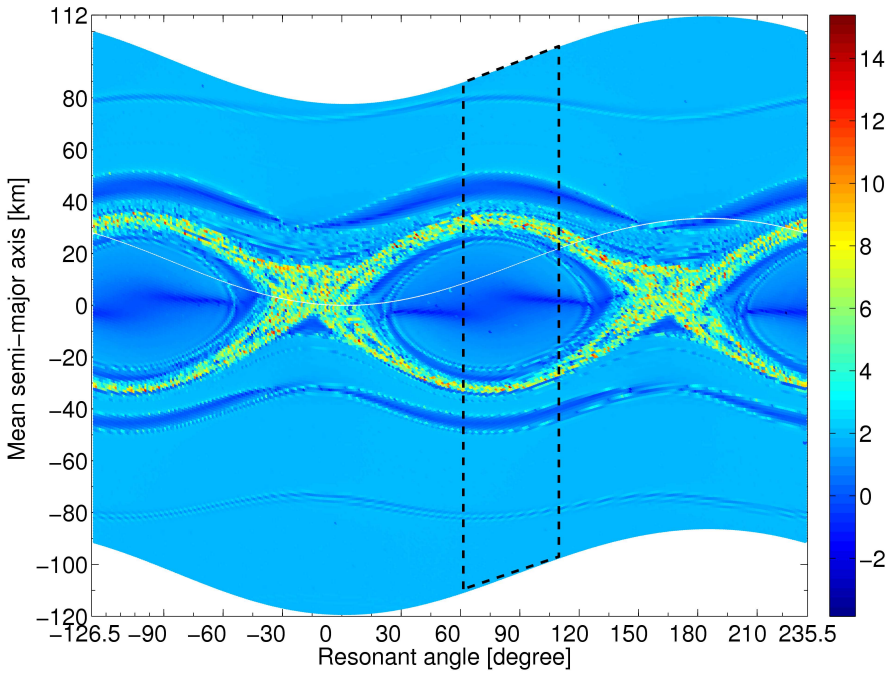

Fig. 13. The MEGNO computed as a function of initial mean longitudes λ_0 and semi–major axis a_0. The equations of motion include the central body attraction, the second degree and order harmonics J_2, C_{22} and S_{22} as well as the luni-solar perturbations. The mean longitude grid is 1° and the semi-major axis grid is 1 km, spanning the 42164±100 km range. The initial conditions are $e_0 = 0.002$, $i_0 = 0.004$, $\Omega_0 = \omega_0 = 0$. The area-to-mass ratio is $A/m = 10$ m^2/kg. Time at epoch is 25 January 1991.

resonant angle section span the complete range in semi-major axis and passes next to the stable equilibrium point. For each orbit defined on this section, we computed the MEGNO indicator and in Figure 14 (middle) we report this value at the end of the simulation as a function of the semi-major axis.

To double check our results, we performed a frequency analysis investigation (see Laskar 1990, 1995 and Noyelles et al. 2008) aimed to study the behaviour of the proper frequency of the resonant angle σ, whose results are reported in Figure 14 (bottom). Here one can clearly remark the distinctive characteristics regarding the well-know 1:1 resonance between the mean longitude and the sidereal time. Indeed, both the MEGNO and the fundamental period show distinctively a minimum close to the stable equilibrium point. In this case, as previously mentioned in Section 4, the MEGNO should slowly converge to $\overline{Y}(t) = 2$ everywhere except at the equilibrium point where the limit value is $\overline{Y}(t) = 0$, that's why, using a finite integration time, we obtain such V-shaped curve, close to 0 in the center of the resonance and to 2 on the borders. It is also worth noting that the fundamental period of σ is reported to be close to 2.25 years, which is in good agreement with the well-known 818 days libration

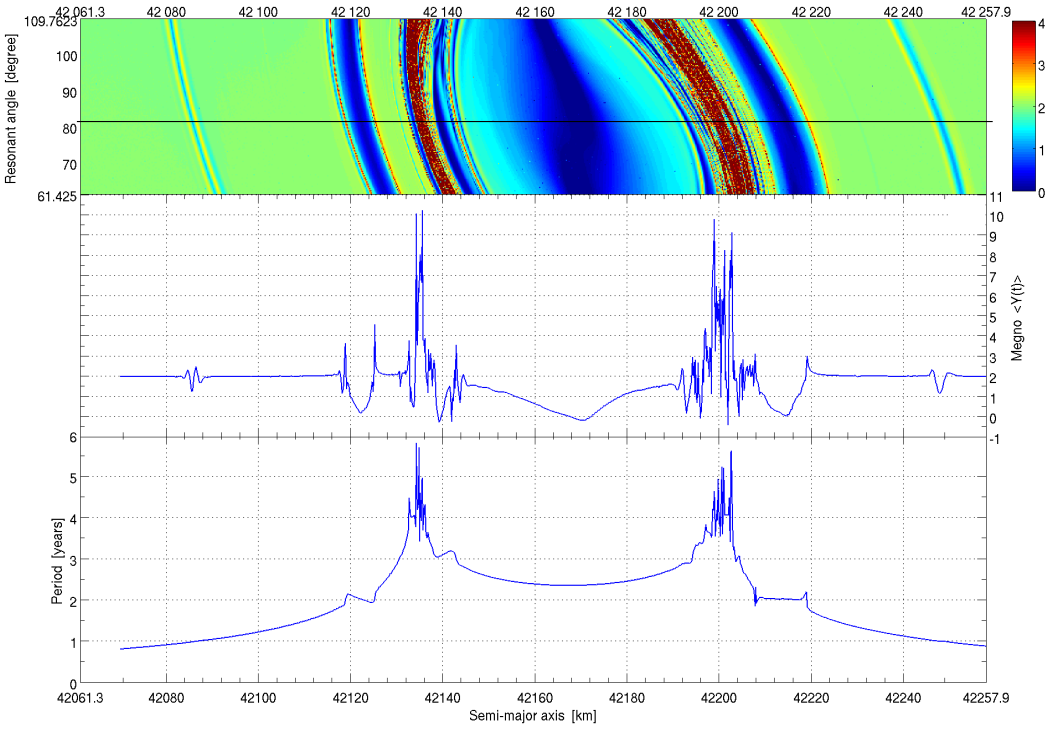

Fig. 14. Blow-up of the phase space with the specification of a *resonant angle section* (horizontal black solid line), that is the set of orbits having the same (osculating) initial resonant angle value, near the first stable equilibrium, namely $\sigma_0^{section} = 81.67°$ (top panel). Evolution of the `MEGNO` with respect to the initial semi-major axis a_0 for the specified section (middle panel). The fundamental period of σ with respect to the initial semi-major axis a_0, computed by means of frequency analysis for the specified section (bottom panel). The estimation of the periods are made over a 20 years period of time.

period of a typical uncontrolled near-geosynchronous object. Near the separatrices, the `MEGNO` clearly presents some obvious high values which confirms the presence of chaotic orbits. Here, the fundamental period reaches significant values and is as a matter of fact not well determined, once again supporting the result of the existence of a chaotic zone.
Moreover the use of frequency analysis allows us to strongly support the hypothesis that the additional patterns are actually related to ***secondary resonances***. Indeed, if we look at the evolution of the fundamental period with respect to the semi-major axis, it is clear that the so-called secondary resonances are associated, regarding the angle σ, with periods which are commensurate with 1 year. More precisely, the major secondary resonance located at approximately 40 km on both sides of the pendulum-like pattern are related to a 2 years fundamental period of σ. Concerning the farther patterns located at ± 80 km, the fundamental period of σ turns out to be very close to 1 year.

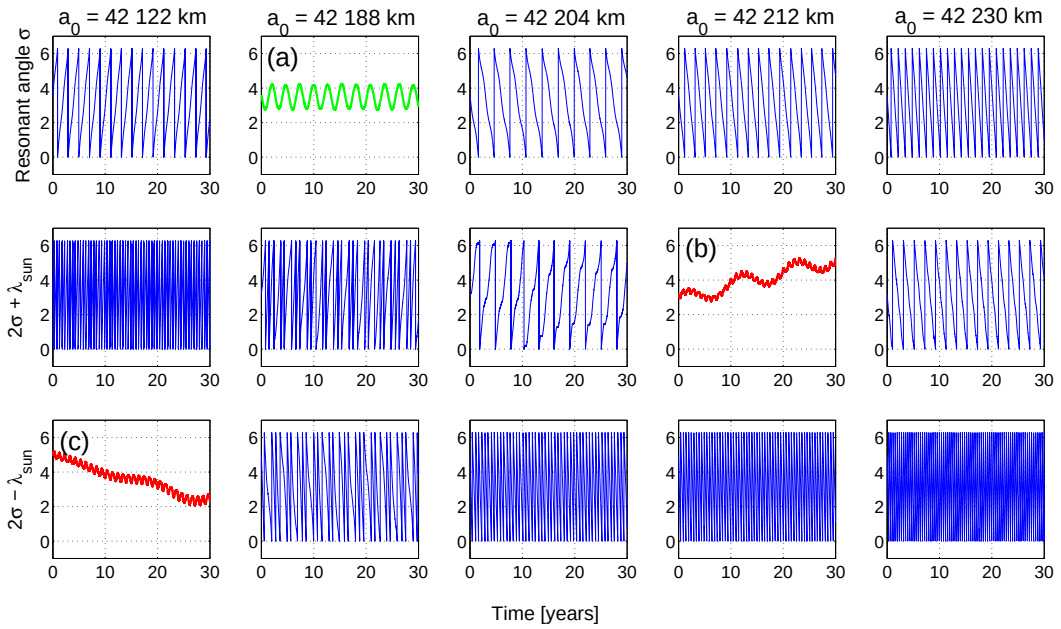

Fig. 15. Time evolution of the angles σ, $2\sigma+\lambda_\odot$ and $2\sigma-\lambda_\odot$ (in radians) for several semi-major axes. In the lower major secondary resonance, $a_0 = 42\,122$ km. In the eye of the principal resonance, $a_0 = 42\,188$ km. Between the primary resonance and the upper secondary resonance, $a_0 = 42\,204$ km. Inside the upper major secondary resonance, $a_0 = 42\,212$ km. Outside the upper major secondary resonance, $a_0 = 42\,230$ km.

As a consequence, we can presumably assume that these before-mentioned secondary resonances are actually related to a commensurability between σ and the 1 year period angle $\lambda_\odot$, that is the ecliptic longitude of the Sun.

To justify this assumption, we focused our attention to the major secondary resonances located at ± 40 km on both sides of the pendulum-like pattern, considering the time-evolution of various linear combinations between σ and $\lambda_\odot$. For this purpose, we considered various initial semi-major axes in the phase space. The results are shown in Figure 15. At first glance, it is apparent that three propagations stand apart from others. In the first row of Figure 15, that is regarding the evolution of the resonant angle σ, we clearly identify the well-know characteristics related to the primary resonance. In particular, in Figure 15a, that is when considering an initial semi-major axis inside the primary resonant (a_0 =42 188 km), σ shows a well-known long-periodic libration (2.25 years) whereas σ circulates outside this region. Furthermore, what is of special interest is the time evolution of both $2\sigma + \lambda_\odot$ and $2\sigma - \lambda_\odot$ shown in the second and third row, respectively. It is clear that most of the time, these angles show a significant circulation regime. However, when considering an initial semi-major axis inside the major lower secondary resonance for $2\sigma - \lambda_\odot$ or similarly inside the major upper secondary resonance for $2\sigma + \lambda_\odot$, both these angles show a significant long-term evolution (Figure 15b,c).

The presence and the location of these secondary resonances can be studied using an appropriate simplified model. Hence we model the averaged geostationary motion by a pendulum-like system, given by its Hamiltonian formulation (Valk et al., submitted for publication) up to order e^2 in the series expansion

$$\mathcal{H} = -\frac{\mu^2}{2L^2} - \dot{\theta} L + 3\,\frac{\mu^4}{L^6}\,R_e^2\,\left(1 - \frac{5}{2}\,e^2\right)\,S_{2200}(\Omega, \omega, M, \theta)\,,$$

where

$$L = \sqrt{\mu a} \qquad \text{and} \quad S_{2200}(\Omega, \omega, M, \theta) = C_{22}\cos\,2\sigma + S_{22}\sin\,2\sigma\,.$$

In this context of direct solar radiation pressure, we can introduce the factor $\mathcal{Z}$ proportional to A/m through the eccentricity e (for further details, we refer to the averaged simplified analytical model developed in Valk et al. (2008). In first approximation, the time evolution of both the eccentricity e and the longitude of perigee ϖ were found to be (neglecting the obliquity of the Earth with respect to the ecliptic)

$$\begin{aligned} e\cos\varpi &= \frac{\mathcal{Z}}{L\,n_\odot}\cos\lambda_\odot + \alpha_0\,, \\ e\sin\varpi &= \frac{\mathcal{Z}}{L\,n_\odot}\sin\lambda_\odot - \beta_0\,, \end{aligned}$$

which introduces $\lambda_\odot$ in the Hamiltonian. The quantity $n_\odot$ is the mean motion of the Sun and both α_0 and β_0 are related to initial conditions with respect to the eccentricity and the longitude of perigee). The resulting Hamiltonian takes the generic form

$$\mathcal{H} = -\frac{\mu^2}{2L^2} - \dot{\theta} L + \frac{F}{L^6}\,\cos\left(2\sigma - 2\sigma_0\right) - \frac{G}{L^6}\,2\cos\left(2\sigma - 2\sigma_0\right)\,\cos\left(\lambda_\odot + \delta\right),$$

where δ, F, G, σ_0 are constants. A suitable transformation is then necessary to introduce action-angle variables (ψ, J) in the libration and in the circulation region of the double pendulum, in such a way any trajectory of the double pendulum is characterized by a constant action J and a corresponding constant frequency $\dot{\psi}$. Rewriting the perturbed system (because of $\lambda_\odot$ terms) by means of these new variables and then using the expansions in Bessel functions, we could isolate any resonance of the type $k\psi \pm \lambda_\odot$, in the circulation region, for any $|k|$ and in the libration region, for $|k| \geq 3$ which corresponds to our frequency analysis. This analysis is surely promising, but it exceeds from the goals of this paper, that's way further investigations will be detailed in a forthcoming publication.

7 Conclusions

The predictability of high area-to-mass ratio space debris located near the geosynchronous region was investigated by means of a recent variational chaos indicator called the MEGNO. Thanks to this technique, we clearly identified the regular (stable) and irregular (chaotic) orbits. This efficient method allowed us to obtain a clear picture of the phase space, hence showing that chaotic regions can be particularly relevant, especially for very high area-to-mass ratios objects. Moreover, we discussed the importance of both the initial eccentricity and time at epoch in the appearance of chaos.

Finally, we brought to the fore a relevant class of additional unexpected patterns which were identified as secondary resonances, that were numerically studied by means of both the MEGNO criterion and frequency map analysis, to eventually conclude that they involve commensurabilities between the primary resonant angle and the ecliptic longitude of the Sun. We also presented an analytical scheme that could explain their existence, that will be discussed in full details elsewhere.

Acknowledgement

The authors thank S. Breiter for helpful discussions about both the MEGNO criterion as well as numerical issues which led to substantial improvement of the present paper, also providing some useful references. Finally, we are grateful for the opportunity to use the frequency analysis tools developed by B. Noyelles and A. Vienne.

References

Anselmo, L., Pardini, C., Orbital evolution of geosynchronous objects with high area-to-mass ratios. In: Danesy, D. (Ed.), Proceedings of the Fourth European Conference on Space Debris, (ESA SP-587). ESA Publications Division, Noordwijk, The Netherlands, pp. 279–284, 2005.

Barrio, R., Borczyk, W., Breiter, S., Spurious structures in chaos indicators maps. Chaos, Solitons & FractalsDoi:10.1016/j.chaos.2007.09.084, 2007.

Benettin, G., Galgani, L., Giorgilli, A., Strelcyn, J.-M., Lyapunov characteristic exponents for smooth dynamical systems and for hamiltonian systems; a method for computing all of them. part 1: Theroy. Meccanica 15, 9–20, 1980

Breiter, S., Wytrzyszczak, I., Melendo, B., Long-term predictability of orbits around the geosynchronous altitude. Advances in Space Research 35, 1313–1317, 2005.

Bulirsh, R., Stoer, J., Numerical treatment of ordinary differential equations by extrapolation methods. Numerische Mathematik 8, 1–13, , March 1966.

Chao, C. C., Analytical investigation of geo debris with high area-to-mass ratio. In: Proceedings of the 2006 AIAA/AAS Astrodynamics Specialist Conference. Keystone, Colorado, AIAA Paper, No. AIAA-2006-6514, , 2006.

Cincotta, P. M., Giordano, C. M., Simó, C., Phase space structure of multi-dimensional systems by means of the mean exponential growth factor of nearby orbits. Physica D 182, 151–178, 2003.

Cincotta, P. M., Simó, C., Simple tools to study global dynamics in non-axisymmetric galactic potentials - i. Astronomy and Astrophysics, Supplement 147, 205–228, 2000.

Cunningham, L. E., On the computation of the spherical harmonics terms needed during the numerical integration of the orbital motion of an artificial satellite. Celestial Mechanics 2, 207–216, 1970.

Deprit, A., Canonical transformations depending on a small parameter. Celestial Mechanics 1, 12–30, 1969.

Goździewski, K., Bois, E., Maciejewski, A. J., Kiseleva-Eggleton, L., Global dynamics of planetary systems with the `MEGNO` criterion. Astronomy and Astrophysics 378, 569–586, 2001.

Goździewski, K., Breiter, S., Borczyk, W., The long-term stability of extrasolar system hd37154. numerical study of resonance effects. Monthly Notices of the RAS 383, 989–999, 2008.

Henrard, J., On a perturbation theory using lie transforms. Celestial Mechanics 3, 107–120, 1970.

Laskar, J., The chaotic motion of the solar system. a numerical estimate of the size of the chaotic zones. Icarus 88, 266–291, 1990.

Laskar, J., Introduction to frequency map analysis. In: Proceedings of 3DHAM95 NATO Advanced Institute. Vol. 533. S'Agaro, pp. 134–150, June 1995.

Lemoine, F. G., Kenyon, S. C., Factor, J. K., Trimmer, R., Pavlis, N. K., Chinn, D. S., Cox, C. M., Klosko, S. M., Luthcke, S. B., Torrence, M. H., Wang, Y. M., Williamson, R. G., Pavlis, E. C., Rapp, R. H., Olson, T. R., The development of the joint nasa gsfc and nima geopotential model egm96. Tech. rep., NASA, TP-1998-206861, 1987.

Liou, J.-C., Weaver, J. K., Orbital evolution of geo debris with very high area-to-mass ratios. The Orbital Quarterly News 8 issue 3, The NASA Orbital Debris Program Office, 2004.

Liou, J.-C., Weaver, J. K., Orbital dynamics of high area-to-mass ratio debris and their distribution in the geosynchronous region. In: Danesy, D. (Ed.), Proceedings of the Fourth European Conference on Space Debris (ESA SP-589). ESA Publications Division, Noordwijk, The Netherlands, pp. 285–290, 2005.

Noyelles, B., Lemaître, A., Vienne, A., Titan's rotation. a 3-dimensional theory. Astronomy and Astrophysics 475, 959–970, 2008.

Schildknecht, T., Musci, R., Flury, W., Kuusela, J., de Leon, J., de Fatima Dominguez Palmero, L., Optical observations of space debris in high-altitude orbits. In: Danesy, D. (Ed.), Proceedings of the Fourth European Conference on Space Debris, ESA SP-587. ESA Publications Division, Noordwijk, The Netherlands, pp. 113–118, 2005.

Schildknecht, T., Musci, R., Ploner, M., Beutler, G., Flury, W., Kuusela, J., Leon Cruz, J., de Fatima Dominguez Palmero, L., Optical observations of space debris in geo and in highly-eccentric orbits. Advances in Space Research 34, 901–911, 2004.

Standish, E. M., JPL planetary and lunar ephemeris, de405/le405. JPL Interoffice Memorandum IOM 312.D-98-048, August 1998.

Stoer, J., Bulirsch, R., Introduction to numerical analysis. Springer-Verlag, New York, 1980.

Valk, S., Lemaître, A., Semi-analytical investigations of high area-to-mass ratio geosynchronous space debris including earth's shadowing effects. Advances in Space ResearchDoi:10.1016/j.asr.2008.02.010., 2008.

Valk, S., Lemaître, A., Anselmo, L., Analytical and semi-analytical investigations of geosynchronous space debris with high area-to-mass ratios influenced by solar radiation pressure. Advances in Space Research 41, 1077–1090, 2008.

Valk, S., Lemaître, A., Deleflie, F., Semi-analytical theory of mean orbital motion for geosynchronous space debris under gravitational influence. Advances in Space Research, submitted for publication.

Wisdom, J., Chaotic behavior and the origin of the 3/1 kirkwood gap. Icarus 56, 51–74, 1983.

Wytrzyszczak, I., Breiter, S., Borczyk, W., Regular and chaotic motion of high altitude satellites. Advances in Space Research 40, 134–142, 2007.